Publication Year	2022
Acceptance in OA@INAF	2024-01-24T16:17:58Z
Title	Cosmic-ray-induced H2 line emission: Astrochemical modeling and implications for JWST observations
Authors	Brandt A. L. Gaches; Shmuel Bialy; Thomas G. Bisbas; PADOVANI, Marco; Daniel Seifried; et al.
DOI	10.1051/0004-6361/202244090
Handle	http://hdl.handle.net/20.500.12386/34615
Journal	ASTRONOMY & ASTROPHYSICS
Number	664

Astronomy & Astrophysics manuscript no. main
July 7, 2022

©ESO 2022

Cosmic-ray-induced H_2 line emission

Astrochemical modeling and implications for JWST observations

Brandt A. L. Gaches[1,2★], Shmuel Bialy[3], Thomas G. Bisbas[1,4], Marco Padovani[5], Daniel Seifried[1], and Stefanie Walch[1]

[1] I. Physikalisches Institut, Universität zu Köln, Zülpicher Straße 77, 50937, Köln, Germany
[2] Center of Planetary Systems Habitability, The University of Texas at Austin, USA
[3] Department of Astronomy, University of Maryland, College Park, MD 20742, USA
[4] Department of Physics, Aristotle University of Thessaloniki, GR-54124 Thessaloniki, Greece
[5] INAF–Osservatorio Astrofisico di Arcetri, Largo E. Fermi 5, 50125 Firenze, Italy

Accepted XXX. Received YYY; in original form ZZZ

arXiv:2206.09780v2 [astro-ph.GA] 6 Jul 2022

ABSTRACT

Context. It has been proposed that H_2 near-infrared lines may be excited by cosmic rays and allow for a determination of the cosmic-ray ionization rate in dense gas. One-dimensional models show that measuring both the H_2 gas column density and H_2 line intensity enables a constraint on the cosmic-ray ionization rate as well as the spectral slope of low-energy cosmic-ray protons in the interstellar medium (ISM).

Aims. We aim to investigate the impact of certain assumptions regarding the H_2 chemical models and ISM density distributions on the emission of cosmic-ray induced H_2 emission lines. This is of particular importance for utilizing observations of these lines with the James Webb Space Telescope to constrain the cosmic-ray ionization rate.

Methods. We compare the predicted emission from cosmic-ray induced, rovibrationally excited H_2 emission lines for different one- and three-dimensional models with varying assumptions on the gas chemistry and density distribution.

Results. We find that the model predictions of the H_2 line intensities for the (1-0)S(0), (1-0)Q(2), (1-0)O(2) and (1-0)O(4) transitions at 2.22, 2.41, 2.63 and 3.00 μm, respectively, are relatively independent of the astro-chemical model and the gas density distribution when compared against the H_2 column density, making them robust tracer of the cosmic-ray ionization rate.

Conclusions. We recommend the use of rovibrational H_2 line emission in combination with estimation of the cloud's H_2 column density, to constrain the ionization rate and the spectrum of low energy cosmic-rays.

Key words. ISM: cosmic rays – ISM: lines and bands – Infrared: ISM – Molecular processes

1. Introduction

Low-energy cosmic rays (LECRs) with energies less than 1 GeV play a significant role in driving the thermochemistry of the molecular interstellar medium (ISM) (Dalgarno 2006; Indriolo & McCall 2013). In regions shielded from ultraviolet (UV) radiation, LECRs are the dominant source of ionization. The ionization they provide drives a rich ion-neutral chemistry, leading to the formation of many astronomically important molecules, as well as the initiation of deuteration (Bayet et al. 2011; Caselli & Ceccarelli 2012; Indriolo & McCall 2013; Bialy & Sternberg 2015; Grenier et al. 2015). Further, LECRs provide an important source of heating, and through the ionization fraction regulate the impact of non-ideal magnetohydrodynamic effects such as ambipolar diffusion (Padovani et al. 2020).

Determining the flux of LECRs irradiating molecular clouds is a difficult endeavor. There have been a number of investigations using a range of molecular lines (e.g. Caselli et al. 1998; van der Tak & van Dishoeck 2000; McCall et al. 2002, 2003; Hezareh et al. 2008; Shaw et al. 2008; Ceccarelli et al. 2011; Hollenbach et al. 2012; Indriolo & McCall 2012; Ceccarelli et al. 2014; Podio et al. 2014; Vaupré et al. 2014; Cleeves et al. 2015; Indriolo et al. 2015; Le Petit et al. 2016; Fontani et al. 2017; Neufeld & Wolfire 2017; Favre et al. 2018; Indriolo et al. 2018; Bacalla et al. 2019; Barger & Garrod 2020; Bovino et al. 2020; Redaelli et al. 2021) and gas temperature (e.g. Ivlev et al. 2019) to estimate the cosmic-ray ionization rate (CRIR), denoted as ζ. In diffuse gas, absorption studies of simple molecular ions probe the CRIR. However, dense gas measurements typically rely on astrochemical modeling and thus are prone to a number of degeneracies, in particular the treatment of the CRIR (Gaches et al. 2019).

Recently, Bialy (2020, hereafter B20) proposed a novel method to estimate the LECR flux using H_2 rovibrational line emission. As the primary CR protons penetrate into the cloud they produce a population of secondary electrons which efficiently excite the rovibrational transitions of H_2 (especially of the first vibrational state $v = 1$) resulting in H_2 line emission in the near-IR. As shown by Bialy et al. (2022) and Padovani et al. (2022, hereafter P22), observations of H_2 rovibrational lines may be used to constrain the spectrum of LECRs that is prevailing in the ISM.

The H_2 lines of interest are shown in Table 1, between 2.22 and 3 μm. The James Webb Space Telescope (JWST) will be able to observe these lines with the NIRSPEC instrument simultaneously. The unprecedented observations will enable JWST to determine the CRIR in dense molecular gas where absorp-

---

[★] E-mail: gaches@ph1.uni-koeln.de

tion measurements are difficult. As such, exploring how different model assumptions impact the line predictions is crucial.

The aforementioned previous calculations assumed a fully molecular one-dimensional slab which enabled parameter-space predictions of the H_2 line intensity as a function of the observed H_2 column density, $N_{\rm obs}$. These calculations assumed fully molecular clouds and did not include the effects of FUV photodissociation and an inhomogeneous density structure, which result in regions in the cloud that are partially atomic. In addition, as previous models are one-dimensional, they assume that the observed column density along the LOS and the effective column density that attenuates CRs as they penetrate into the cloud, are identical. In an inhomogeneous three-dimensional cloud, CRs can penetrate from different directions, along "rays" passing through different density profiles (not only along the direction of the LOS), resulting in strong fluctuations in the local CR ionization and excitation rate. Therefore, the role of density structure and chemical evolution model (e.g. equilibrium versus non-equilibrium), should be constrained, as these will impact the conversion of the local quantity (induced H_2 emission) to an integrated quantity (observed H_2 line intensity).

In this paper, we present synthetic H_2 line emission (2D plane-of-the-sky) maps of a realistic molecular cloud irradiated by an interstellar CR proton spectrum. We use the three-dimensional astrochemical models presented in Gaches et al. (2022), which include a prescription for CR attenuation and self-consistently formed molecular clouds from the SILCC-Zoom project (Seifried et al. 2017), and the CR excitation rates computed in P22.

Table 1: H_2 transitions and physical constants

Transition	J_u	J_l	λ (μm)	E_{ul} (eV)	α_{ul}
(1-0)S(0)	2	0	2.22	0.56	0.30
(1-0)Q(2)	2	2	2.41	0.51	0.36
(1-0)O(2)	0	2	2.63	0.47	1.00
(1-0)O(4)	2	4	3.00	0.41	0.34

2. Methods

We model a molecular cloud that is impacted by a flux of cosmic rays, and calculate the resulting H_2 rovibrational excitation and the consequent NIR line emission from the cloud.

2.1. Incident CR flux

For the CRs that are impinging on the cloud surface we assume the interstellar CR proton spectrum from Padovani et al. (2018), with a low-energy spectral slope of $\alpha = -0.8$; this is the "$\mathcal{H}$ model" which provides a good agreement to observations of the CRIR in diffuse clouds.

2.2. CR attenuation

As the CRs penetrate into the cloud they lose energy through ionization, dissociation and excitation. We account for this attenuation process by adopting the depth-dependent CRIR, $\zeta(N_{\rm eff})$, from Table F.1 of Padovani et al. (2018), as well as a depth-dependent H_2 excitation rate, $\zeta_{\rm ex}(N_{\rm eff})$ from P22 (see their Figs. 5, 6 and also Fig. 3 in Bialy et al. 2022). Hereafter we consider a set of cloud models, including 1D slab geometry models, as well as 3D models based on hydro simulations of turbulent clouds, as summarized in Table 2. For our 1D models, $N_{\rm eff}(z) = \mu N'(z)$ where $N'(z) = \int_0^z n dz'$ is the column density from cloud edge to the point of interest at depth z inside the cloud, and $\mu = \cos(\theta)$ is the cosine angle of the B-field lines with the cloud normal. We adopt $\mu = 1$. In our 3D models, we utilize the effective column density by accumulating the column along Healpix rays (Górski et al. 2005),

$$N_{\rm eff}(x,y,z) = -\frac{1}{2.5} \ln \left(\frac{1}{N_\ell} \sum_{i=1}^{N_\ell} {\rm e}^{-2.5 N_i(x,y,z)'} \right), \tag{1}$$

for $N_\ell = 12$ rays at the Healpix $\ell = 0$ level of refinement.

2.3. Density structure

To explore the effect of the cloud structure on the resulting H_2 line emission, we consider five models with different density distributions and chemical properties, as summarized in Table 2.

Models 1 – 3 are one-dimensional slabs. Models 1 and 2 assume a constant density, of $n = 10$ and 10^3 cm^{-3}, respectively. Model 3 has a variable density profile in which the density and column density at each point in the cloud are related through

$$N_{\rm eff}(z) = 8.05 \times 10^{19} \exp \left[1.6 \left(\frac{n}{\rm cm^{-3}} \right)^{0.12} \right] {\rm cm^{-2}}. \tag{2}$$

This relies on the empirical $A_{\rm V} - n$ relation found by Bisbas et al. (2019) and Bisbas et al. (in prep) based on a series of turbulent ISM box simulations and galaxy disk simulations. For the densities significant for our results, this relationship well reproduces the average densities as a function of effective column density (see Fig. 5 of Gaches et al. (2022)). This relationship is for a Solar metallicity gas, and can change with metallicity (Hu et al. 2021). Appendix A provides additional details on the 1D astrochemical models.

We also use two three-dimensional density distributions (Models 4 and 5). Model 4 uses the density distribution and astrochemical model from Gaches et al. (2022), which was also previously used in Bisbas et al. (2021). This cloud (called "dense" cloud) is a subregion from the larger-scale simulations of Wu et al. (2017). The "dense" cloud is located in a cube with uniform resolution of 112^3 cells, a side length $L = 13.88$ pc, total mass $M_{\rm tot} = 5.9 \times 10^4$ $M_\odot$, and mean H-nucleus density $\langle n \rangle = 640$ cm^{-3} (see Wu et al. 2017 and Bisbas et al. 2021 for more details). Model 5 is a molecular cloud from the magneto-hydrodynamic (MHD) SILCC-Zoom simulations (Seifried et al. 2017, 2020). These simulations model zoomed-in regions of the stratified disk SILCC simulations (Walch et al. 2015; Girichidis et al. 2016) with the initial Galactic-scale magnetic field set to 3 μG and uses the Flash 4.3 MHD code (Fryxell et al. 2000). The SILCC-Zoom MHD cloud is located in a cube with side length, $L \approx 125$ pc with a total mass, $M_{\rm tot} = 2.13 \times 10^5$ $M_\odot$.

2.4. Astrochemical Models

For Models 1 – 4, the chemistry is computed with a modified version of the public astrochemistry code 3d-pdr (Bisbas et al. 2012; Gaches et al. 2022). We use a reduced network derived from the UMIST 2012[1] chemical network database (McElroy et al. 2013) consisting of 33 species and 330 reactions. The chemistry is then evolved to steady-state using an integration time of 10 Myr.

---

[1] `http://udfa.ajmarkwick.net`

Table 2: Physical and chemical models

	Model	Density	FUV	CR Attenuation	Code	Notes
1D	1	Constant $n = 10$ cm^{-3}	1	✓	3D-PDR	
	2	Constant $n = 10^3$ cm^{-3}	1	✓	3D-PDR	
	3	Variable $N_{\rm eff} - n$	1	✓	3D-PDR	Following Eq. (2)
3D	4	Variable Simulation	10	✓	3D-PDR	Wu et al. (2017); Bisbas et al. (2021)
	5	Variable Simulation	1.4		Flash	SILCC-Zoom, Seifried et al. (2017)

Models 1 – 3 use an external FUV radiation field of $G_0 = 1$ (normalized to the spectral shape of Habing 1968) to minimize the impact of photochemistry and Model 4 uses $G_0 = 10$ to be consistent with previous studies (Bisbas et al. 2021; Gaches et al. 2022).

Model 5 uses non-equilibrium chemistry with a network of 7 species (Glover & Mac Low 2007a,b; Glover et al. 2010; Glover & Clark 2012), a constant atomic hydrogen CRIR $\zeta = 3 \times 10^{-17}$ s^{-1} and an external FUV radiation field $G_0 = 1.4$. The effective column density is computed and stored during the simulation as described above using the TreeRay/OpticalDepth module (Clark et al. 2012; Walch et al. 2015; Wünsch et al. 2018). Due to the use of a constant CRIR, the chemistry is not entirely self-consistent with our treatment of the excitation rate, as described below. However, the ionization rates we consider are not high enough to greatly impact the H_2 abundances. Therefore, our main results will not be significantly altered by this assumption.

2.5. H_2 excitation and line emission

In steady state, the flux of secondary electrons becomes independent of the local density (see Ivlev et al. 2021). Thus, we can use the calculation of the excitation rate $\zeta_{\rm exc,u}$ from P22 for $v_u = 1$, $J_u = 0, 2$. For the "$\mathcal{H}$" cosmic-ray flux model, the excitation rate varies from 10^{-15} to 10^{-16} s^{-1} between the cloud surface and interior (see Fig. 5 in P22). This calculation uses the CR energy loss function assuming a fully molecular gas. In practice, the loss function should account for a mix of atomic and molecular hydrogen, however as we show in the appendix, this has a marginal impact on our results for $N_{\rm obs} > 10^{21}$ cm^{-2} (see Figure A.1).

Given, $\zeta_{\rm exc,u}$, the emissivity for a specific H_2 line is

$$\epsilon_{ul} = \alpha_{ul}\frac{E_{ul}}{4\pi}\zeta_{\rm exc,u}n({\rm H_2})\,, \tag{3}$$

where α_{ul} is the probability that the excitation of state (v_u, J_u) will be followed by radiative decay to state (v_l, J_l), E_{ul} is the transition energy, and $n({\rm H_2})$ is the H_2 number density. The α_{ul} factor does not include collisional quenching as the densities we consider lie below the critical density (e.g., $n_{\rm crit} \approx 10^{11}$ cm^{-3} at 100 K; Bialy 2020). Our models assume H_2 is entirely in the para-state, which is applicable for the dense regions were are primarily concerned with (Flower et al. 2006, see Appendix A for an exploration of the impact of a different ortho-to-para ratio).

The line-of-sight integrated line intensity is then:

$$F_{ul}(x, y) = \int_0^L \epsilon_{ul}(x, y, z)e^{-\sigma_d N'(x,y,z)}{\rm d}z\,, \tag{4}$$

where $N'(x, y, z) = \int_0^z n(x, y, z'){\rm d}z'$ is the cumulative column density along the line of sight, from the cloud edge to a point inside the cloud (at depth z), L is the cloud size, and $\sigma_d = 4.5 \times 10^{-23}$ cm^2 is the NIR dust absorption cross section per hydrogen nuclei (B20, Draine 2003). Hereafter, we also define the *total* column density integrated along the LOS, $N_{\rm obs} \equiv \int_0^L n(x, y, z'){\rm d}z'$. Similarly, $N_{\rm obs}({\rm H_2})$ is the LOS-integrated column density of H_2.

3. Results

Figure 1 shows the line intensity of the denoted H_2 line, seen along the z-axis, for Models 4 (top) and 5 (bottom). The observed fluctuations in the line intensities correspond to density fluctuations in the cloud, as well as variations in the effective column density. The emission saturates at high column densities due to the obscuration of dust. We note that these clouds formed through different processes: the Model 4 cloud is the product of a cloud-cloud collision and the Model 5 cloud is likely the result of supernova shells interacting and contains structures on larger length scales, and thus also more diffuse gas.

Figure 2 shows the line intensities as a function of the total integrated column of hydrogen nuclei, $N_{\rm obs}$, for our three-dimensional models (models 4,5) and the $N_{\rm eff} - n$ 1D model (model 3). We find that these models rapidly diverge for $N_{\rm obs} < 10^{22}$ cm^{-2}. The divergence is caused by the substantial differences in H-H_2 chemical structure. In particular, Model 5 is more diffuse than Model 4, and while both Models 3 and 5 evolve the chemistry to steady state, Model 4 evolves the chemistry with a non-equilibrium solver. As such, the models exhibit different H_2 abundance distributions, driving the divergence at low column densities.

The impact of different H_2 abundance distributions can be factored out by comparing the H_2 line intensity versus the H_2 column density. Figure 3 shows the logarithmic column density bin-averaged line intensity as a function of $N_{\rm obs}({\rm H_2})$ to investigate whether the differences in chemistry evolution, and thus the abundance profiles, are a dominant factor. We find that now the agreement between the Models 3, 4, 5 is strong. We also compare our results to the P22 model (solid curve) which assumes a constant density, purely molecular slab. Despite the different treatments of the chemistry and density distributions in the various models, there is a good agreement on the line intensity as a function of $N_{\rm obs}({\rm H_2})$. We also show the observational upper limits from B20, which are consistent with the various models presented.

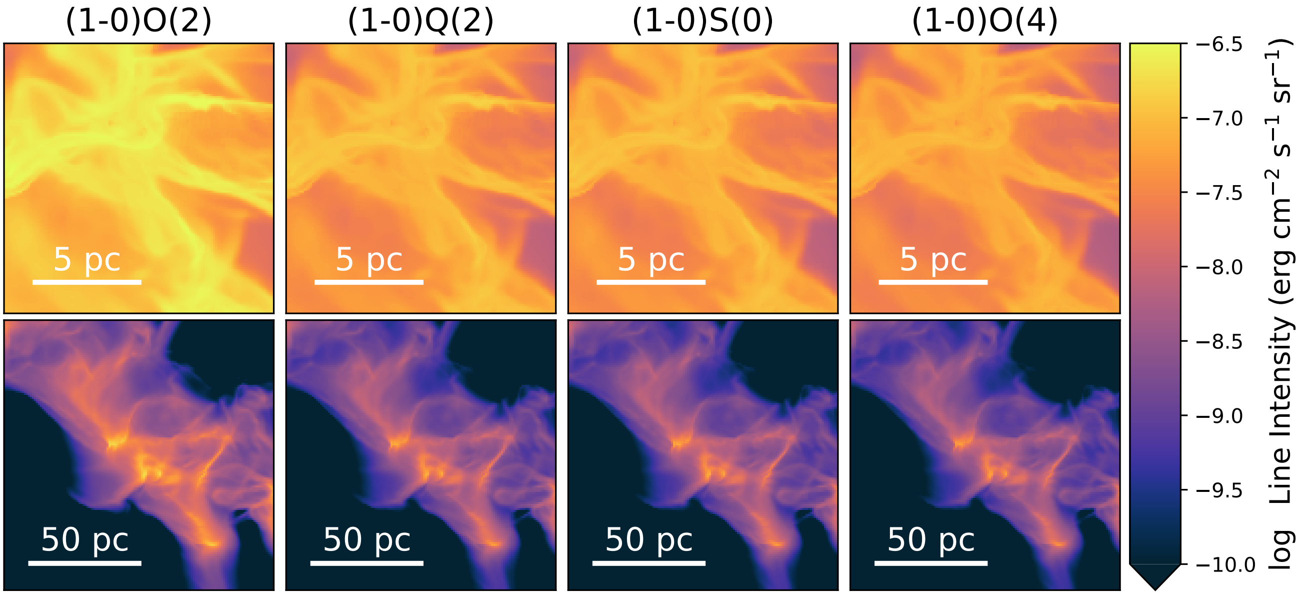

Fig. 1: Line-of-sight line intensities of the 3D-PDR model (top; Model 4) and SILCC-Zoom MHD cloud (bottom; Model 5) for the four different H_2 lines in Table 1.

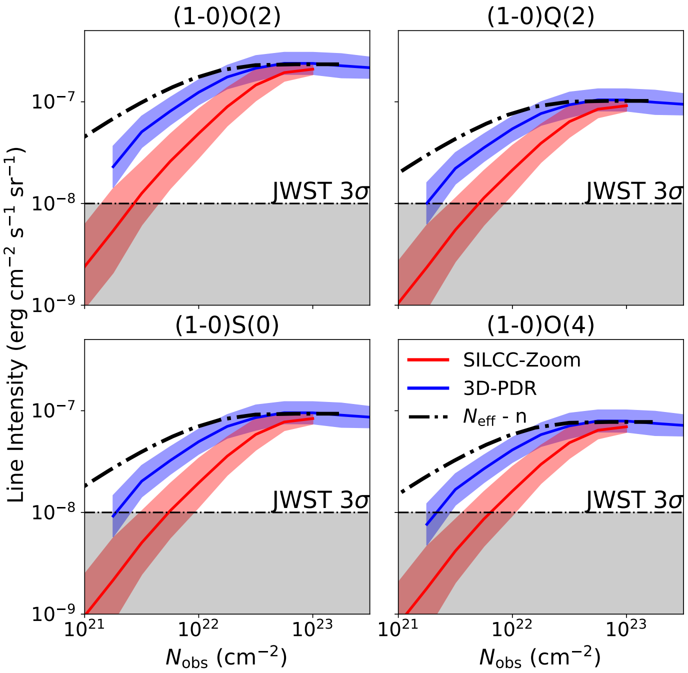

Fig. 2: Logarithmic column-density bin-averaged line intensities versus the total H-nucleus column density, $N_{\rm obs}$ for the H_2 lines in Table 1. The blue and red lines correspond to Models 4 and 5, respectively with the filled regions representing $\pm 2\sigma$. Black dashed-dot line shows the results for model 3. The shadowed region shows the JWST sensitivity with a signal-to-noise ratio of 3 with 1.25 h of integration and 50 shutters (P22).

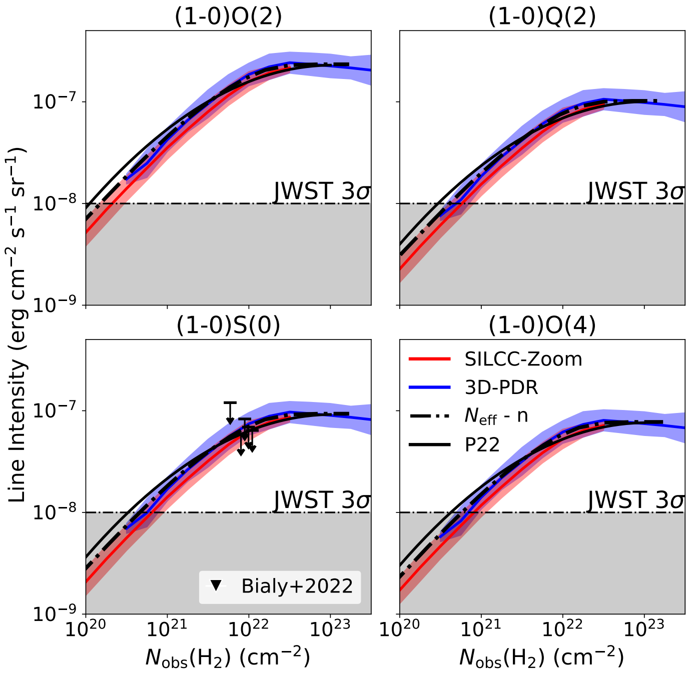

Fig. 3: Same as Fig. 2 but plotted against the line-of-sight H_2 column density, $N_{\rm obs}(H_2)$. Black solid line corresponds to the calculation in P22. Black triangles show the observational upper limits on the (1-0)S(0) line from Bialy et al. (2022).

4. Conclusions

The results presented in this paper demonstrate that the assumptions regarding geometry, chemical evolution and density distribution do not play a significant role when the H_2 column density is used along with the H_2 emission lines for constraining the CRIR. However, if the H_2 column density is not constrained, and the total hydrogen column density $N_{\rm obs}$ is used instead, then the various models diverge in their prediction of the H_2 line intensity, especially at low columns, $N_{\rm obs} < 10^{22}$ cm^{-2}. This is because the various models assume different density distributions and chemical evolution which result in different H-H_2 abundances.

There are a few chemical effects not included in this study which will be investigated in future work. First, we focused primarily here on the role of CRs. However, X-rays can also excite the H_2 lines through secondary electrons produced by X-ray ionizations, in a similar manner as CRs. Second, the H_2 excitation rate and emission assume the H_2 is primarily in the para-H_2 state. However, at low column densities, particularly in regions with enhanced radiation, this assumption may begin to break down (Flower et al. 2006). As a result, at low column densities, there may be variations in the H_2 line depending on the ortho-to-para ratio and whether or not state-specific chemistry is included (see Appendix A for a model using an approximate treatment of the ortho-to-para ratio). Third, we have neglected additional H_2 excitation processes, such as FUV photo-excitation at the cloud envelopes, and H_2 formation pumping. As shown in B20 (see their Fig. 1, and Eqs. 10, 11) this assumption is valid for clouds sufficiently high in CRIRs or low in FUV irradiation. A comprehensive 3D model that includes these additional H_2 excitation mechanisms will be presented in a future work.

To summarize, we have presented synthetic CR induced H_2 line emission maps of four key emission lines (Table 1) for two simulated three-dimensional molecular clouds and several one-dimensional models. These lines are of particular importance: B20 and P22 predicted that they trace the CRIR in dense gas and can be simultaneously observed using NIRSPEC on the JWST. We find that the H_2 line intensity as a function of the H_2 column density is relatively insensitive to the assumed density distribution or chemical model. Due to this insensitivity, we recommend the use of the H_2 lines in Table 1 for constraining the CRIR in dense gas, in particular using the JWST.

Acknowledgements. BALG, DS, and SW acknowledge support by the Deutsche Forschungsgemeinschaft (DFG) via the Collaborative Research Center SFB 956 “Conditions and Impact of Star Formation”. TGB acknowledges support from Deutsche Forschungsgemeinschaft (DFG) grant No. 424563772. SB acknowledges support from the Center for Theory and Computations (CTC) at the University of Maryland. The following PYTHON packages were utilized: NUMPY (Harris et al. 2020), SCIPY (Virtanen et al. 2020), MATPLOTLIB (Hunter 2007), CMOCEAN. This research has made use of NASA’s Astrophysics Data System.

References

Bacalla, X. L., Linnartz, H., Cox, N. L. J., et al. 2019, A&A, 622, A31
Barger, C. J. & Garrod, R. T. 2020, ApJ, 888, 38
Bayet, E., Williams, D. A., Hartquist, T. W., & Viti, S. 2011, MNRAS, 414, 1583
Bialy, S. 2020, Communications Physics, 3, 32
Bialy, S., Belli, S., & Padovani, M. 2022, A&A, 658, L13
Bialy, S., Burkhart, B., & Sternberg, A. 2017, ApJ, 843, 92
Bialy, S. & Sternberg, A. 2015, MNRAS, 450, 4424
Bialy, S. & Sternberg, A. 2016, ApJ, 822, 83
Bisbas, T. G., Bell, T. A., Viti, S., Yates, J., & Barlow, M. J. 2012, MNRAS, 427, 2100
Bisbas, T. G., Schruba, A., & van Dishoeck, E. F. 2019, MNRAS, 485, 3097
Bisbas, T. G., Tan, J. C., & Tanaka, K. E. I. 2021, MNRAS, 502, 2701
Bovino, S., Ferrada-Chamorro, S., Lupi, A., Schleicher, D. R. G., & Caselli, P. 2020, MNRAS, 495, L7
Caselli, P. & Ceccarelli, C. 2012, A&A Rev., 20, 56
Caselli, P., Walmsley, C. M., Terzieva, R., & Herbst, E. 1998, ApJ, 499, 234
Ceccarelli, C., Dominik, C., López-Sepulcre, A., et al. 2014, ApJ, 790, L1
Ceccarelli, C., Hily-Blant, P., Montmerle, T., et al. 2011, ApJ, 740, L4
Clark, P. C., Glover, S. C. O., & Klessen, R. S. 2012, MNRAS, 420, 745
Cleeves, L. I., Bergin, E. A., Qi, C., Adams, F. C., & Öberg, K. I. 2015, ApJ, 799, 204
Dalgarno, A. 2006, Proceedings of the National Academy of Science, 103, 12269
Draine, B. T. 2003, ARA&A, 41, 241
Favre, C., Ceccarelli, C., López-Sepulcre, A., et al. 2018, ApJ, 859, 136
Flower, D. R., Pineau Des Forêts, G., & Walmsley, C. M. 2006, A&A, 449, 621
Fontani, F., Ceccarelli, C., Favre, C., et al. 2017, A&A, 605, A57
Fryxell, B., Olson, K., Ricker, P., et al. 2000, ApJS, 131, 273
Gaches, B. A. L., Bisbas, T. G., & Bialy, S. 2022, A&A, 658, A151
Gaches, B. A. L., Offner, S. S. R., & Bisbas, T. G. 2019, ApJ, 878, 105
Girichidis, P., Walch, S., Naab, T., et al. 2016, MNRAS, 456, 3432
Glover, S. C. O. & Clark, P. C. 2012, MNRAS, 421, 116
Glover, S. C. O., Federrath, C., Mac Low, M. M., & Klessen, R. S. 2010, MNRAS, 404, 2
Glover, S. C. O. & Mac Low, M.-M. 2007a, ApJS, 169, 239
Glover, S. C. O. & Mac Low, M.-M. 2007b, ApJ, 659, 1317
Górski, K. M., Hivon, E., Banday, A. J., et al. 2005, ApJ, 622, 759
Grenier, I. A., Black, J. H., & Strong, A. W. 2015, ARA&A, 53, 199
Habing, H. J. 1968, Bull. Astron. Inst. Netherlands, 19, 421
Harris, C. R., Millman, K. J., van der Walt, S. J., et al. 2020, Nature, 585, 357
Hezareh, T., Houde, M., McCoey, C., Vastel, C., & Peng, R. 2008, ApJ, 684, 1221
Hollenbach, D., Kaufman, M. J., Neufeld, D., Wolfire, M., & Goicoechea, J. R. 2012, ApJ, 754, 105
Hu, C.-Y., Sternberg, A., & van Dishoeck, E. F. 2021, ApJ, 920, 44
Hunter, J. D. 2007, Computing in Science & Engineering, 9, 90
Indriolo, N., Bergin, E. A., Falgarone, E., et al. 2018, ApJ, 865, 127
Indriolo, N. & McCall, B. J. 2012, ApJ, 745, 91
Indriolo, N. & McCall, B. J. 2013, Chemical Society Reviews, 42, 7763
Indriolo, N., Neufeld, D. A., Gerin, M., et al. 2015, ApJ, 800, 40
Ivlev, A. V., Silsbee, K., Padovani, M., & Galli, D. 2021, ApJ, 909, 107
Ivlev, A. V., Silsbee, K., Sipilä, O., & Caselli, P. 2019, ApJ, 884, 176
Le Petit, F., Ruaud, M., Bron, E., et al. 2016, A&A, 585, A105
McCall, B. J., Hinkle, K. H., Geballe, T. R., et al. 2002, ApJ, 567, 391
McCall, B. J., Huneycutt, A. J., Saykally, R. J., et al. 2003, Nature, 422, 500
McElroy, D., Walsh, C., Markwick, A. J., et al. 2013, A&A, 550, A36
Neufeld, D. A. & Wolfire, M. G. 2017, ApJ, 845, 163
Padovani, M., Bialy, S., Galli, D., et al. 2022, A&A, 658, A189
Padovani, M., Ivlev, A. V., Galli, D., & Caselli, P. 2018, A&A, 614, A111
Padovani, M., Ivlev, A. V., Galli, D., et al. 2020, Space Sci. Rev., 216, 29
Podio, L., Lefloch, B., Ceccarelli, C., Codella, C., & Bachiller, R. 2014, A&A, 565, A64
Redaelli, E., Sipilä, O., Padovani, M., et al. 2021, A&A, 656, A109
Seifried, D., Haid, S., Walch, S., Borchert, E. M. A., & Bisbas, T. G. 2020, MNRAS, 492, 1465
Seifried, D., Walch, S., Girichidis, P., et al. 2017, MNRAS, 472, 4797
Shaw, G., Ferland, G. J., Srianand, R., et al. 2008, ApJ, 675, 405
Sternberg, A., Le Petit, F., Roueff, E., & Le Bourlot, J. 2014, ApJ, 790, 10
van der Tak, F. F. S. & van Dishoeck, E. F. 2000, A&A, 358, L79
Vaupré, S., Hily-Blant, P., Ceccarelli, C., et al. 2014, A&A, 568, A50
Virtanen, P., Gommers, R., Oliphant, T. E., et al. 2020, Nature Methods, 17, 261
Walch, S., Girichidis, P., Naab, T., et al. 2015, MNRAS, 454, 238
Wu, B., Tan, J. C., Nakamura, F., et al. 2017, ApJ, 835, 137
Wünsch, R., Walch, S., Dinnbier, F., & Whitworth, A. 2018, MNRAS, 475, 3393

Appendix A: One-dimension astrochemical models

We use three different density distributions: constant $n = 10, 10^3$ cm^{-3} and one following the $N_{\rm eff} - n$ relation of Eq. (2). Cosmic-ray attenuation is included following the prescription given in Gaches et al. (2022), where the hydrogen nuclei column density, $N_{\rm eff}$ is equated with the attenuating column and the ionization rate follows the polynomial fit of the "$\mathcal{H}$ model" from Padovani et al. (2018), as described above.

Figure A.1 shows the hydrogen nuclei number density and H_2 abundance, $x(H_2) \equiv n(H_2)/n$, as a function of hydrogen nuclei column density, $N_{\rm eff}$. The models exhibit a transition from predominantly atomic H to molecular H_2, gas with increasing column density, as the photodissociating FUV radiation is absorbed in the H_2 lines and in the dust (for the $n = 10^3$ cm^{-3} this transition occurs at small columns, beyond the x-axis lower limit), (Sternberg et al. 2014; Bialy & Sternberg 2016; Bialy et al. 2017).

Fig. A.2 shows that as a function of the total hydrogen column density, the line intensity show significant variation between the models. Figure A.3 shows the line flux as a function of the H_2 column density for the one dimensional astrochemical models and exhibits far less variation. The constant density model with $n = 10^3$ cm^{-3} is fully molecular and best matches the P22 predictions which assumed a fixed H_2 abundance, $x(H_2) = 0.5$. The $N_{\rm eff} - n$ model line intensities are dimmer than the $n = 10$ cm^{-3} model at low column densities due to the lower H_2 abundances in this limit. As functions of the H_2 column density, all one dimensional models are in agreement to within an order of magnitude, and consistent with the Bialy et al. (2022) upper limits.

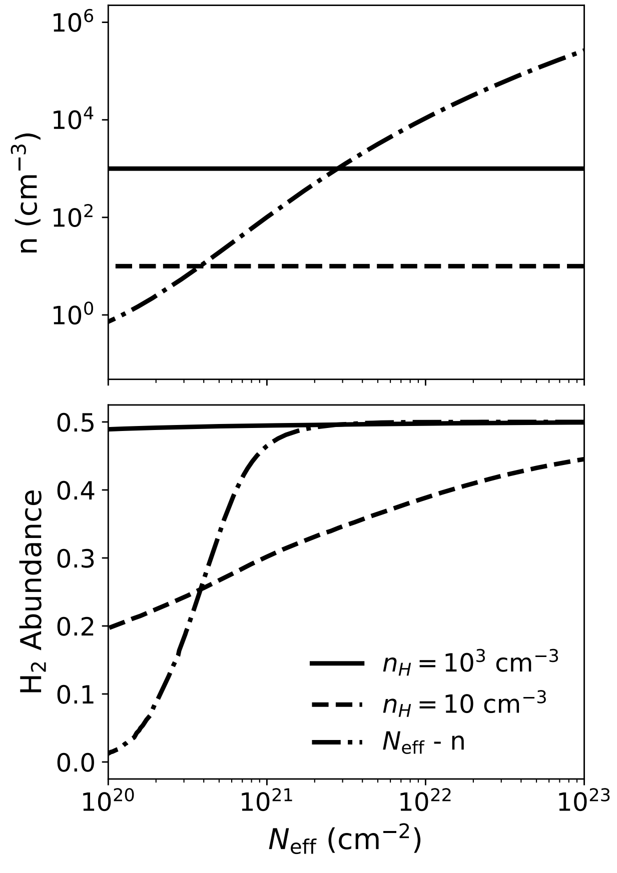

Fig. A.1: Total gas density (top) and H_2 abundance (bottom) versus total hydrogen nuclei column density, $N_{\rm eff}$ for three different one-dimensional 3D-PDR models.

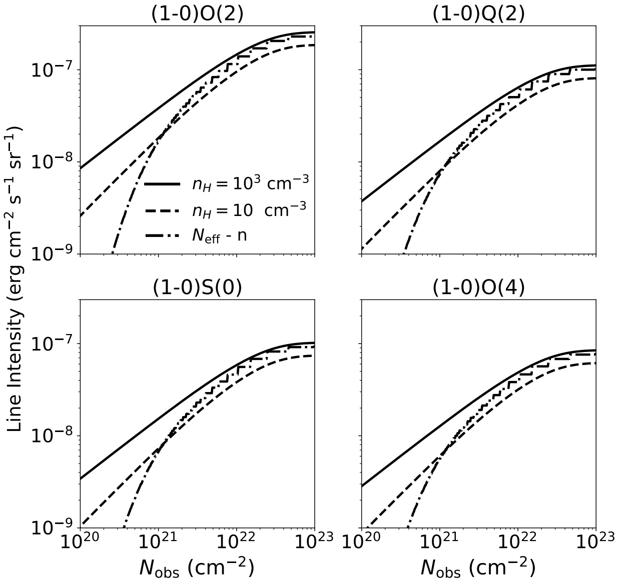

Fig. A.2: Same as Figure A.3 but plotted against the total observed column density, $N_{\rm obs}$.

In our fiducial models, we assume a metallicity of $Z = 1.0 Z_\odot$ and that the H_2 is entirely in the para-H_2 spin state. We ran an additional set of four models using the $N_{\rm eff} - n$ density distribution. Three models use different metallicities: $Z = 0.1 Z_\odot$, $Z = 0.5 Z_\odot$, and $Z = 2.0 Z_\odot$ and the fourth uses $Z = 1.0 Z_\odot$ but assumes the H_2 ortho-to-para ratio (OPR) is in thermal equilibrium (Flower

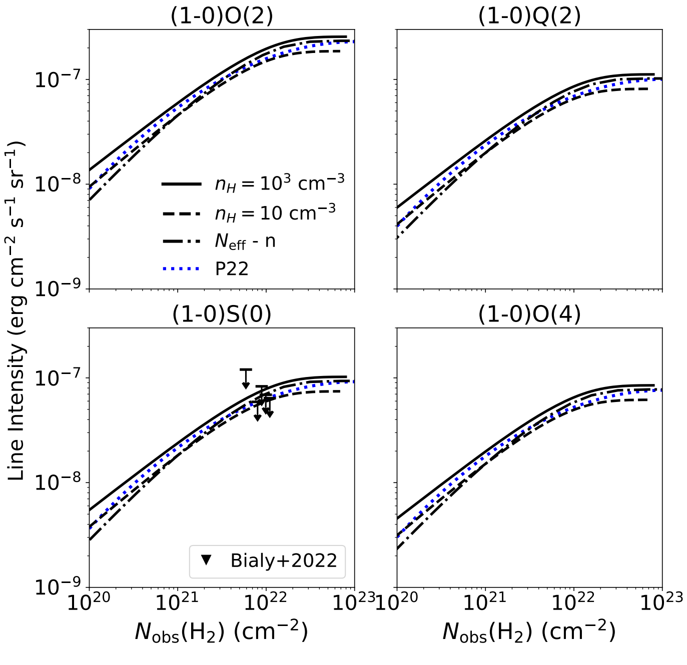

Fig. A.3: Line intensity as a function of H_2 column density for the four H_2 lines considered in this work. Blue dotted line corresponds to the calculation in P22. Black triangles show the upper limits on the (1-0)S(0) line from Bialy et al. (2022).

et al. 2006),

$$\mathrm{OPR} = 9\exp(-170.5/T_g), \tag{A.1}$$

where T_g is the gas temperature computed by 3D-PDR and was computed in post-processing for the H_2 emission since 3D-PDR does not include spin chemistry. This relationship deviates from the expected asymptotic OPR ratio of 3 at high temperatures, but the gas we consider is generally cool (T < 100 K), where this relationship still produces an OPR less than 3. However, the use of this approximation will provide a first indication of the importance of the OPR in determining these line intensities. The H_2 line emissivity is then modified as

$$\epsilon_{ul} = \alpha_{ul}\frac{E_{ul}}{4\pi}\zeta_{\mathrm{exc,u}}\left(\frac{n(\mathrm{H_2})}{1+\mathrm{OPR}}\right). \tag{A.2}$$

The dust opacity and H_2 formation rates are linearly scaled with metallicity. Further, the metallicity impacts the heating and cooling due to the changes in the abundances of metals and dust.

Figure A.4 shows the H_2 line intensities versus H_2 column density for these four different models along with the fiducial $N_{\mathrm{eff}} - n$ model. At low H_2 column densities, there is little deviation, although the "Thermal OPR" model shows a slight decrease in line intensity at low column densities (and thus higher temperatures) due to H_2 also being in ortho-H_2 spin state. At high column densities, the line intensities asymptote to different values due to lower (higher) metallicities have their $\tau_d = 1$ surface deeper (shallower) in the clouds.

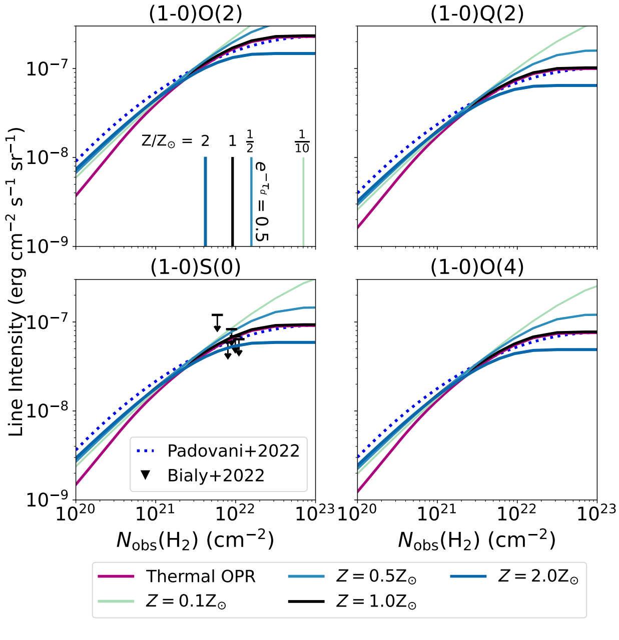

Fig. A.4: Same as Figure A.3 but plotting the $N_{\mathrm{eff}} - n$ model for different metallicities and a model using an ortho-to-para ratio in thermal equilibrium. The vertical lines in the top-left plot denote the H_2 column density where $e^{-\tau_d} = 0.5$.